A Novel Omnidirectional Swimming Robot with Articulated-Compliant Legs

Yaohui Xu[1], Hanlin Li[2], Furui Yu[3], Qiyang Zuo[1], Fengran Xie[4], Xiang Xie[1], and Kai He[1]

***Abstract*—Stability, adaptability, and maneuverability are critical performance indexes for underwater biomimetic robots, especially in narrow spaces. However, these aspects can sometimes be contradictory. This paper presents an omnidirectional swimming robot inspired by the whirligig beetle and designed to achieve good performance in stability, adaptability, and maneuverability. Its design features four novel articulated-compliant robotic legs, and its hydrodynamic model is formulated using Kirchhoff's equation and the Lagrangian method. The hydrodynamic forces are calculated using the quasi-steady flow model, and extensive experiments are carried out to examine thrust generation and speed. It is found that this omnidirectional robot has significant improvements compared to a conventional robot with a single passive joint in its leg. Specifically, its swimming speed is as fast as 0.34 m/s with a frequency of 1.4 Hz, which is a 30.8% increase. Moreover, the robot's multimodal swimming capabilities is demonstrated, such as swimming forward, retreating, lateral swimming to the left or right, zero-radius turning, and no zero-radius turning, by configuring different locomotive patterns of the articulated-compliant legs. The passing and collision experiments demonstrate the robot's potential applications in narrow spaces. Overall, this omnidirectional swimming robot strikes a great balance among stability, adaptability, and maneuverability, providing a promising solution for high-performance underwater vehicles.**

***Index Terms*—Bio-inspired robot, omnidirectional swimming robot, compliant and passive joint, modeling, articulated leg.**

I. Introduction

AUtonomous underwater vehicles (AUVs) show great promise for applications in complex underwater environments, such as rescue operations, monitoring, maintenance, and other challenging missions [1], [2]. Although traditional underwater robots are well-designed and easy to control, and excel in high-speed locomotion [3], [4], they tend to be bulky and insufficiently agile. As a result, they are typically used in relatively spacious and deep underwater environments. In narrow spaces, AUVs have obvious drawbacks in terms of maneuverability and adaptability. Moreover, the noise and high power consumption of traditional propellers further limit their usability.

Comparatively, biomimetics has great advantages in robotic design [5]–[7], where biological organisms are assessed as a basis for robotic development [8]–[10]. Compared with traditional propeller-driven robots, those designed with a bionic approach demonstrate better performance in terms of locomotive efficiency, energy density [11], and maneuverability [12]. Furthermore, bionic-inspired robots are capable of accomplishing extremely complex missions that are inaccessible to traditional robots, such as collective behaviors [13] and accessing regions for disease inspection or treatment that are difficult to reach [14]. Robots with bionic elements show great potential for underwater applications, with fins [15], [16], paddles [17], [18], and flippers [19] that mimic fish, frogs, turtles, and other aquatic species being proposed.

However, the adaptability of robots in narrow spaces is currently limited by designs that simply mimic specific traits or behaviors of creatures [20]–[22]. Besides, the asymmetric actuation of some robots can affect their own yaw stability. For example, robotic fish are unable to turn without a radius when encountering obstacles, despite their fast swimming speed. While they may be only suitable for wider underwater environments, their gait deficiency may hinder movement through narrow spaces. Furthermore, the caudal fin's shaking of the robotic fish's body reduces yaw stability. However, the robot's yaw stability can be improved by using symmetric flapping. Furthermore, by swimming in various gait patterns, such as retreating, turning with zero-radius, or lateral swimming, the robot's flexibility, adaptability, and performance in difficult scenarios can be improved. These capabilities primarily result from more complex local coordination among limbs, which is most common in humans and other complex mammals facing stressful situations. Therefore, it is worth considering using leg coordination to expand the range of robot applications in more narrow and complex underwater environments [23]. This study adopts symmetric flapping and improves leg coordination to

Manuscript received: December 6, 2022; Revised: February 10, 202; Accepted: June 26, 2023.

This letter was recommended for publication by Editor Pauline Pounds upon evaluation of the reviewers' comments. This work was supported by (the Shenzhen Science and Technology Program (JCYJ20220531100807016), Guangdong Basic and Applied Basic Research Foundation (2023A1515011152), SIAT-CUHK Joint Laboratory of Precision Engineering and Shenzhen Polytechnic Research Fund (6023310032K).)

[1]Yaohui Xu, Qiyang Zuo, Xiang Xie and Kai He are with the Shenzhen Institute of Advanced Technology, Chinese Academy of Sciences, Shenzhen 518055, China, and also with the University of Chinese Academy of Sciences, Beijing 100049, China. e-mail: yh.xu@siat.ac.cn, qy.zuo@siat.ac.cn, x.xie@siat.ac.cn, kai.he@siat.ac.cn.(Corresponding author: Kai He)

[2]Hanlin Li is with College of Mechanical Engineering, Yanshan University, Qinhuangdao 066004, China, and Shenzhen Institute of Advanced Technology, Chinese Academy of Sciences, Shenzhen 518055, China. email: hl.li1@siat.ac.cn

[3]Furui Yu is with College of Mechanical and Electrical Engineering, Shaanxi University of Science & Technology, Xi'an 710021, China, and Shenzhen Institute of Advanced Technology, Chinese Academy of Sciences, Shenzhen 518055, China. email: fr.yu@siat.ac.cn

[4]Fengran Xie is with the School of Artificial Intelligence, Shenzhen Polytechnic, Shenzhen 518055, China. email: xiefengran@szpt.edu.cn

Digital Object Identifier (DOI): see top of this page.

enhance the gait of underwater robots, thereby improving their yaw stability and adaptability.

A passive concept is adopted in the design of legs to achieve better coordination. This method is preferred because it offers simplicity in fabrication and control, along with higher efficiency. The passive method was initially proposed for fin design [24], and since then, a growing number of legs or fins have been designed using this method and applied in underwater robotic platforms [25], [26]. While most fins or legs feature only one passive joint [27], [28], this design has the drawback of a large passive joint angle that does not quickly recover to zero at the start of the power stroke. This results in a simple design but at the expense of efficiency and net thrust. Enhancing recovery speed could improve the net force and propulsive efficiency. However, this aspect is still rarely explored. Therefore, this paper proposes a novel drag-based leg to increase the net force and efficiency, which will further enhance the robot's maneuverability.

This study has three main contributions, as follows: (a) A novel biomimetic approach is proposed for designing a unique underwater omnidirectional robot with four legs. A symmetric flapping approach is used to ensure good yaw stability. The robot has multiple modes, including retreating, lateral swimming, and zero-radius turning, facilitated by the leg's cooperation. These modes help the robot perform better in terms of adaptability and maneuverability when dealing with challenging environments. (b) This paper proposes a novel leg design with a rigid link and three rigid plates articulated by flexible passive joints to improve the net force and propulsive efficiency. A comparison between the proposed leg and the traditional leg design with just a single passive joint is made, revealing the advantages of the proposed leg in terms of net thrust, efficiency, and swimming speed. (c) Varieties of swimming modes are presented in a water tank. The passing and collision experiments are also completed. This study presents an innovative and alternative scheme in robotic design that focuses on challenging underwater environments, such as narrow spaces.

The rest of this paper is arranged as follows. Design of the omnidirectional swimming robot is presented in Section II, followed by dynamic modeling in Section III. Swimming robot prototype and experimental setup are described in Section IV. The results and discussions are shown in Section V. Finally, Section VI includes the conclusions and suggestions for future work.

II. Design of the Omnidirectional Robot

Whirligig beetles are notable for their rapid swimming on the water's surface due to their two pairs of articulated and paddle-like legs [29]. As shown in Fig. 1(a), each leg comprises four segmented appendages, including metacoxa, femur, tibia, and tarsus, which are linked by three joints. Muscles control each segment of the leg independently [30]. Furthermore, stoppers are located on one side of the leg near the joint to limit the rolling angle during the power stroke, ensuring that there is enough area of the leg. Stopper elements are also crucial for effective protection when whirligig beetles face unexpected conditions [31]. Many hairs adhere to the surface of the legs. Moreover, as shown in Fig. 1(b), the leg spreads flat during the power stroke, and the hairs expand to enhance the effective area and boost net thrust. During the recovery stroke, which is contrary to the power stroke, the leg bends, and hairs shrink to reduce resistance force. The leg deforms throughout the power and recovery strokes, creating effective thrust that enables whirligig beetles to move quickly. Also, whirligig beetles employ symmetric flapping to adapt to harsh aquatic environments for higher speed, as elaborated in [30]. Although the lateral force created by this mode minimally impacts forward swimming, it considerably enhances stability and maneuverability [32].

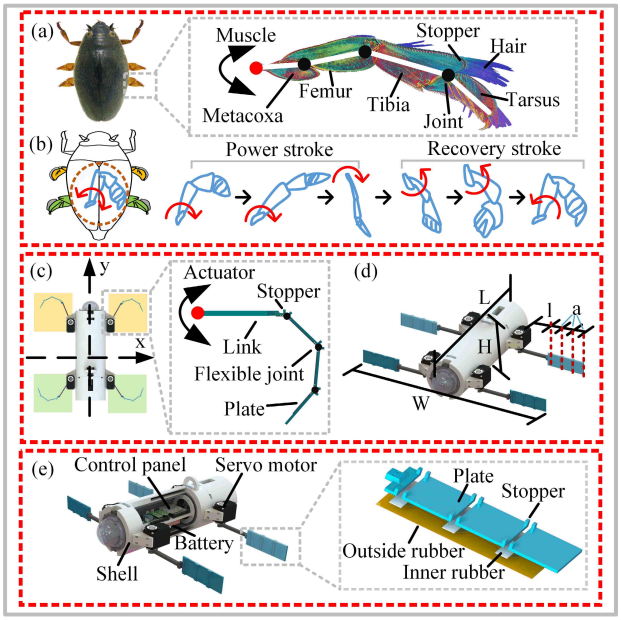

Fig. 1. The bionic design of swimming robot. (a) the whirligig beetle and the structure of its legs (b) the motion of whirligig beetle's leg in one swimming stroke (c) the swimming robot and leg inspired by whirligig beetle (d) the design specifications of the swimming robot. (e) the fabrication of the swimming robot and its legs.

Effective thrust, stability, adaptability, and maneuverability of a swimming robot depend largely on its articulated legs with hairs and its symmetric propulsive mode. However, due to the difficulty in fabrication, the hairs are often ignored, and leg design and its symmetric layout become the primary focus. This paper primarily focuses on the leg design and its symmetric layout in the swimming robot, enhancing its gaits and adaptability in narrow areas. The approach uses a front-to-back symmetry layout, instead of the traditional left-to-right symmetry, based on configurable modes, as shown in Fig. 1(c). This new symmetry layout allows the swimming robot to adopt various gaits, such as lateral swimming, retreating, or zero-radius turning. To provide more details, all the gaits and their significance are explained in Fig. 8 in Section V and in the accompanying material (Movie S1. (1), (2)). The robot's leg consists of four segments, a thin link, and three paddle-like rigid plates connected by three passive joints. Stoppers are attached to one side of the rigid plates. Although the first joint of the leg is active, the others are passive, utilizing fewer

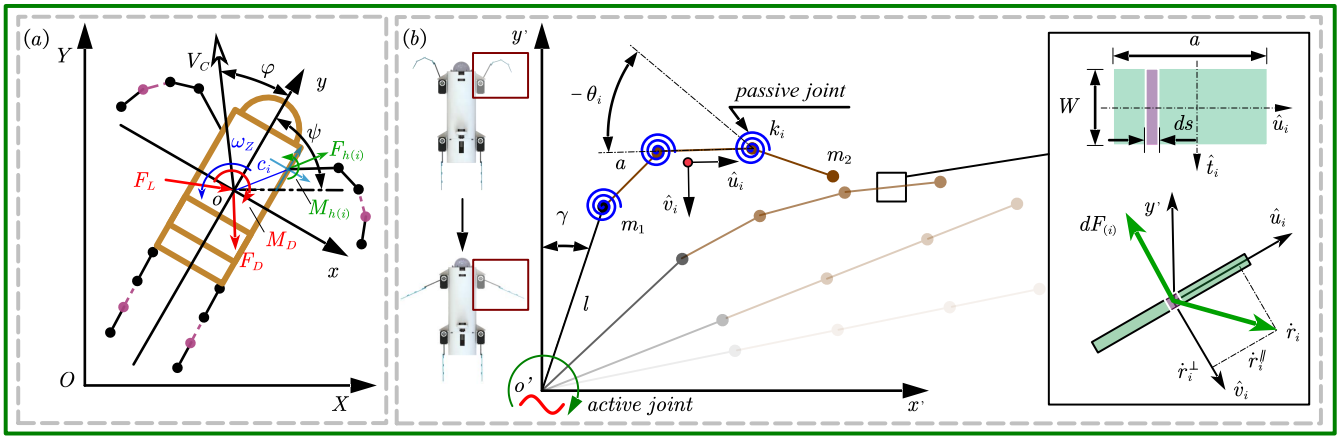

Fig. 2. The dynamic model of swimming robot. (a) top view of the swimming robot actuated by front leg with multiple flexible passive joints in planar motion (b) schematic diagram of leg with multiple flexible passive joints.

actuators and simplifying the collaboration between the legs. During the recovery stroke, the leg bends at passive joints, reducing resistance due to fluid interaction. The bent legs immediately go flat at the start of the power stroke to provide more thrust, and they remain flat until the stroke ends, thanks to the stoppers on one side. This passive method reduces the mechanical complexity, size, weight, and power consumption of the swimming robot, making it more efficient and effective.

Fig. 1(d) shows the design parameters of the swimming robot and its leg. The robot's length, width, and height are denoted as L, W, and H, respectively, while the link and plate lengths are denoted by l and a, respectively. These parameters are presented in TableI. Fig. 1(e) illustrates the fabrication process of the robot, where the control panel and battery are protected by the robot's shell with sealing rings. The paddle-like rigid plates have two layers of flexible rubber adhered to them with glue. The thickness of the inner rubber varies to meet the stiffness requirements of each joint. The outside thin rubber is added to improve adhesion of the inner rubber to the paddle-like plates. A separate DYNAMIXEL XXW540 waterproof servo motor controls each leg of the bio-inspired swimming robot. Also, the robot's orientation is measured using a single inertial measurement unit (IMU) mounted on the control panel.

TABLE I: Parameters of the swimming robot.

parameter	value	meaning
L	426 (mm)	*Body length*
W	569 (mm)	*Body width*
H	110 (mm)	*Body height*
m_b	2.5 (Kg)	*Body mass*
J_{bz}	0.07 (Kg/m^2)	*Body inertia about z−axis*
N	3	*Leg joint number*
l	105 (mm)	*Link length*
a	35 (mm)	*Plate length*
k_1	0.05 $(N.m/rad)$	*First joint stiffness*
k_2	0.04 $(N.m/rad)$	*Second joint stiffness*
k_3	0.02 $(N.m/rad)$	*Last joint stiffness*
C_n	1.3	*Drag coefficient*
m_1	0.016 (Kg)	*Link mass of the leg*
m_2	0.01 (Kg)	*Mass of each plate*
c_i $(i = 1-4)$	144 (mm)	*Distance between robot center and leg*
m_{ax}, m_{ay}, J_{az}	*ignored*	*Mass added influence*

III. Dynamic Modeling

A. Modeling of the Swimming Robot

As noted in Section II, the swimming robot in this study has four legs, and no more than two legs are actuated for each mode. The forward swimming gait is used to create the dynamic model, as shown in Fig. 2(a). Kirchhoff's equation from traditional marine vessel technologies is used to compute the dynamics of the swimming robot. The heave motion, roll motion, and pitch motion are all unimportant when the swimming robot swims in the plane XOY. As a result, three rigid body movements remain: the surge motion ($V_C x$), the sway motion ($V_C y$), and the yaw motion (ω_z). The rigid body's motion in the xoy plane can be described as follows:

$$(m_b - m_{ax})\,\dot{V}_{Cx} = (m_b - m_{ay})\,V_{Cy}\omega_z + F_{ext-x} \quad (1)$$

$$(m_b - m_{ay})\,\dot{V}_{Cy} = (m_b - m_{ax})\,V_{Cx}\omega_z + F_{ext-y} \quad (2)$$

$$(J_{bz} - J_{az})\,\dot{\omega}_z = (m_{ax} - m_{ay})\,V_{Cx}V_{Cy} + M_{ext-z} \quad (3)$$

As shown in Fig. 2, components of the external force and torque exerted on the rigid head, F_{ext-x}, F_{ext-y}, M_{ext-z}, can be obtained as,

$$F_{ext-x} = F_{hx} + F_D \sin\varphi + F_L \cos\varphi \quad (4)$$

$$F_{ext-y} = F_{hy} - F_D \cos\varphi + F_L \sin\varphi \quad (5)$$

$$M_{ext-z} = M_{hz} + M_D \quad (6)$$

where F_{hx} is the projection of the force of four legs (F_h) exerted onto the rigid body by the legs about x-axis, F_{hy} is the projection of the force F_h exerted onto the rigid body by the legs about y-axis, M_{hz} is the projection of the torque exerted onto the rigid body by the legs about z-axis, F_L is the lift force, F_D is the drag force, M_D is the drag moment. F_L and F_D could be calculated according to [33]. F_h and M_{hz} can be represented as:

$$F_h = \sum_{i=1}^{4} F_{h(i)} \tag{7}$$

$$M_{hz} = \sum_{i=1}^{4} \left(M_{h(i)} - c_i \times F_{h(i)} \right) \tag{8}$$

where F_h and M_{hz} are the force vector and torque exerted onto the rigid body by all legs.

B. Modeling of Leg

In this Section, we focus on thrust of proposed leg. A serial of parameters are chosen, as seen in Fig. 2(b). The Lagrangian method is employed to obtain the dynamics of this mechanism. The proposed leg is depicted as a multi-segmented linkage linked by flexible joints that act as torsion springs [34], as seen in Fig. 2(b). The mass is assumed at the end of each segment. The differentiation of hydrodynamic force $dF_{(i)}$ at each segment can be represented as:

$$dF_{(i)}(s,t) = -0.5 C_n \rho W \left(\dot{r}_i^{\perp} \right)^2 ds \tag{9}$$

where $\dot{r}_i^{\perp}$ is the velocity component normal to the plate unit axis, and C_n is obtained from the experiments. ρ is the density of the fluid.

The position vector of the point at the $j-th$ link of the rowing leg with respect to the $i-th$ joint is:

$$^{i}r_j = r_j(x) - r_{i-1}(a) \tag{10}$$

The torque exerted by the hydrodynamic force at the $j-th$ link of the rowing leg with respect to the $i-th$ joint is:

$$i_j = ^{i} r_j \times dF_{(i)} \tag{11}$$

The non-conservative torque with respect to the $i-th$ joint of the rowing leg is:

$$\tau_i = -k_i \theta_i + \sum_{j=i}^{N} \int_0^a i_j(x)\, dx \tag{12}$$

This paper assumed that k_i would be infinity when θ_i is equal to zero. Finally, motions of the leg can be obtained as:

$$M(Q)\ddot{Q} + V\left(Q, \dot{Q}\right) = \tau \tag{13}$$

We denote $Q = [q_1, q_2, ..., q_{N+1}]^T = [\gamma, \theta_1, \theta_2, ..., \theta_N]^T$, where γ is the angle of motor. [35] described the calculating method of M and V in detail.

The non-conservative torque of the rowing leg at each joint is:

$$\tau = [\tau_1, \tau_2, ..., \tau_N]^T \tag{14}$$

The nonlinear aspect of the fluid-structure interaction force is captured by the modeling of the swimming robot and leg. The kinematics and dynamics of the swimming robot and leg provide a solid foundation for understanding the relationship between leg deformation and net thrust or efficiency, as well as the advantages of robot speed.

IV. The Swimming Robot Prototype and Experimental Setup

The experimental setup, depicted in Fig. 3, consists of a water tank, a traditional bionic leg with a single passive joint (LSPJ), and the proposed leg with three passive joints (LTPJ), as seen in Fig. 3(a). A force sensor is attached to the water tank's frame to measure the leg's thrust, as shown in Fig. 3(b). The motor actuation power source is set to 12V, and a high-speed camera is mounted above the water tank to record motion images. To simulate narrow spaces, a cuboid frame is placed in the water tank, as shown in Fig. 3(c). Passing and collision experiments are completed within this frame.

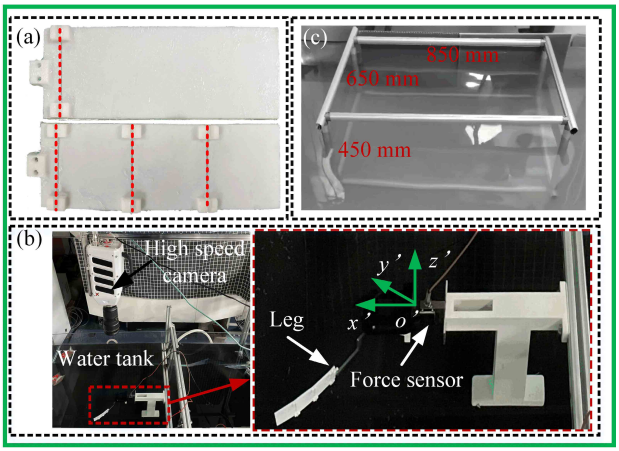

Fig. 3. Experimental setup. (a) the paddle used in experiments (b) high speed camera and force measurement of the leg (c) a cuboid frame in the water tank.

Oscillatory motions of the leg with different amplitudes and frequencies are tested. During these tests, we track the current consumption, angular deformation at the passive joint, and force change over time. Experimental data for the LTPJ and LSPJ are compared to comprehend how the thrust changes throughout the entire stroke and to confirm the proposed leg's design and dynamic model. A lower smoothing technique is applied to eliminate the noisy data, and we use five seconds of continuous oscillatory motion to obtain mean values. To explore the propelling force and electric consumption relationship, we use the ratio of the propulsive force along the x-axis to electric power consumption [36], which we modify as:

$$\eta = \frac{\int_0^{nT} F_{h(i)}(t) dt}{\int_0^{nT} V\, |I(t)|\, dt} \tag{15}$$

Here, $F_{hi}(t)$ is the propulsive force of a leg, V is the constant voltage, $I(t)$ is the current consumption, and T is the time-period of oscillation, n is the number of T.

The stiffness of torsional spring constant for the passive joint can be evaluated as [37]

$$k_i = \frac{Ewh^3}{12l} \tag{16}$$

where h is the thickness, l is the length, w is the width, and E is the Young's modulus of the flexible material used for the passive joints.

The selection of stiffness is critical for passive joints. In this paper, model simulation is utilized for assessing joint stiffness, because the expense of experiments is considerable. It can be seen from the leg's model that the toque of the joint increases as it gets closer to the actuator. So, in this paper, the closer the passive joint is to the actuator, the larger the stiffness is set. Furthermore, the range of stiffness is measured by monitoring whether or not the motion of the leg is normal. To further explore the stiffness groups, three stiffness gradient groups are chosen, and the average thrust is computed. The group with the highest overall average thrust at frequencies of 0.6 Hz and 1.4 Hz, which are regular motor operating limits, is regarded the best and is used in our robot. The actuator's amplitude is set to $120°$.

A water tank, which is 5.5 m in length, 1.8 m in width, and 1.5 m in height, is used for the robotic swimming experiment. The robot average swimming speed is measured by stopwatch and soft ruler attached on one side of water tank. The PID method is applied in the yaw stability control of the swimming robot which adjusts amplitude of the motor at real time. While, Because the swimming robot receives little thrust during the recovery stroke, the PID technique loses efficiency in this phase, leading the adjustable amplitude to continuously grow until it reaches its limit. As a result, the leg cannot be actuated in the power stroke. Therefore, the limit of adjustable amplitude is set to $5°$ to guarantee leg motion. The experiments with the same parameters are repeated five times.

V. Result and Discussion

A. Experiment of Flapped Leg

Fig. 4 demonstrates the motions of the LTPJ during one oscillation cycle. As observed, the leg bends due to an angle increase at each passive joint during the recovery stroke, effectively reducing the resistant force. Moreover, the leg immediately goes flat at the start of the power stroke, increasing the net leg thrust.

According to Fig. 5, the model closely matches the experimental thrust and angular changing trend. While in Fig. 5(a), the experimental power stroke experiences delayed force due to minimal damping that occurs during oscillation. Conversely, in the model, the influence of the flow velocity created by the previous adjacent power stroke is not considered, resulting in lower drag force during the recovery stroke in the experiment. In Figs. 5(b) and 5(c), each joint's angular change occurs almost simultaneously, reducing resistance during the recovery stroke and increasing thrust during the power stroke. Moreover, the leg is confined beyond the allowable angle during the power stroke due to severe torque and force from the water,

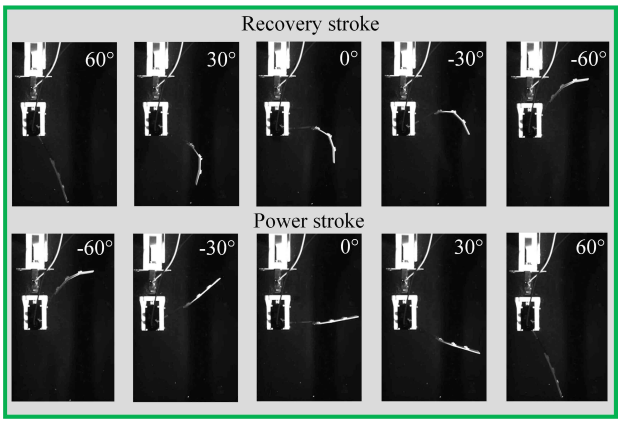

Fig. 4. The image of leg deformation during power stroke and recovery stroke with frequency 0.6 Hz and amplitude $120°$.

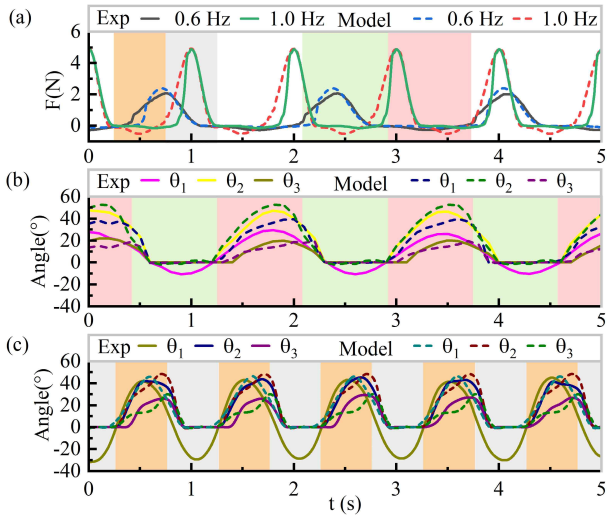

Fig. 5. Comparison of simulated model and experiment with amplitude $120°$. Exp represents experiment data. The power stroke and recovery stroke in 0.6 Hz is indicated with pink region and green region respectively. The power stroke and recovery stroke in 1.0 Hz is indicated with orange region and gray region respectively. (a) thrust comparison (b) angular comparison with 0.6 Hz (c) angular comparison with 1.0 Hz.

causing the angle at the first joint to display some negative values.

Fig. 6 illustrates the mechanism of the LTPJ for increasing thrust. According to Fig. 6(a), the LTPJ outperforms the LSPJ significantly in larger net thrust during the power stroke, which is attributed to the advantage of multiple joints in angle changing speed. As observed in Figs. 6(b), (c), and (d), the largest angle of the LTPJ at 0.6 Hz is $43°$, whereas for the LSPJ, it is $93°$. Likewise, the largest angle of the LTPJ at 1.0 Hz is $42°$, while for the LSPJ, it is $101°$. Each passive joint's largest angle of the LTPJ is less than half that of the LSPJ. Additionally, each passive joint's angles of the LTPJ change almost simultaneously, reducing the conversion time consumption between curved and straight shapes. For instance, in power strokes, t_{c3} is around 0.1s faster than t_{c1}, and t_{c5} is also approximately 0.1s faster than t_{c2}, despite t_{c4} being equal to t_{c2}. The reduced time consumption contributes to the quick

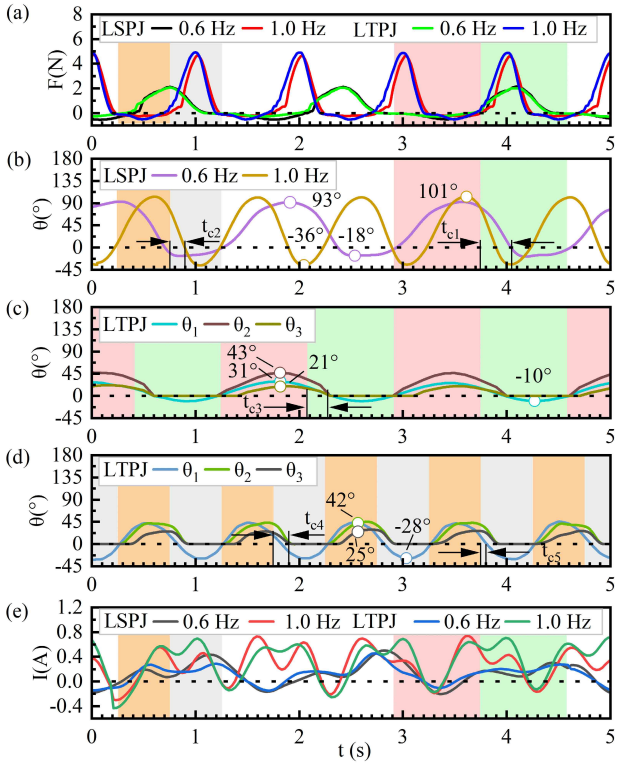

Fig. 6. Experimental comparison between LTPJ and LSPJ with amplitude 120°. The indication of color area is same as Fig. 5. (a) thrust comparison (b) angular variation of LSPJ (c) angular variation of LTPJ with 0.6 Hz (d) angular variation of LTPJ with 1.0 Hz (e) comparison of current's consumption.

increase of effective areas, making the LTPJ outstanding in the rapidly increasing thrust of the power stroke. Moreover, while increasing thrust, the LTPJ's steady-state current consumption is slightly higher than the LSPJ, as shown in Fig. 6(e).

In Fig. 7(a), we compare the average thrust of the two legs, with the LTPJ having a larger net thrust than the LSPJ, and the difference grows as frequency and amplitude increase. In Fig. 7(b), we compare the propulsive efficiency of the two legs to assess the influence of increasing thrust on electric power consumption. It is evident that the LTPJ offers additional benefits, surpassing the LSPJ in terms of efficiency and net thrust without requiring one to swap for the other.

B. Experiment of Swimming Robot with Flapped Leg

Flapping schemes based on the cooperation of different legs with phase offsets have been developed, as shown in Fig. 8. The robot has eight fundamental gaits, including swimming forward and retreating, lateral swimming to the left or right, zero-radius turning, and non-zero-radius turning. All legs produce force in the direction normal to their surface. The leg is actuated with an amplitude of 120° and a frequency of 0.8 Hz.

Moving forward: All legs are symmetric with respect to the mid-line of the body. The front two legs are actuated synchronously, while the rear legs are not driven. Throughout the cycle, the net thrust of the two front legs propels the

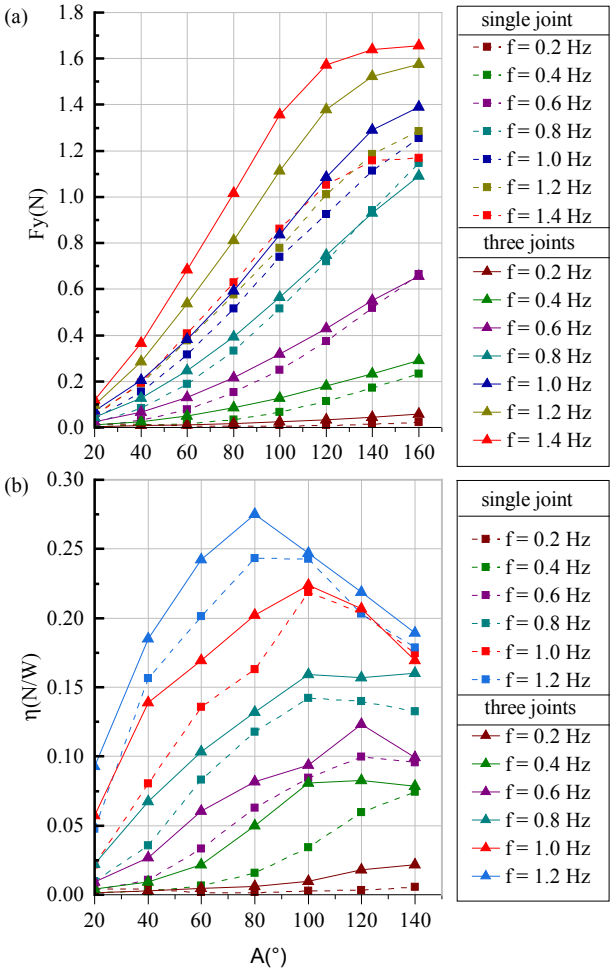

Fig. 7. Comparison of average force and propulsive efficiency between LTPJ and LSPJ (a) experimental results of the average propulsive force (b) experimental results of propulsive efficiency.

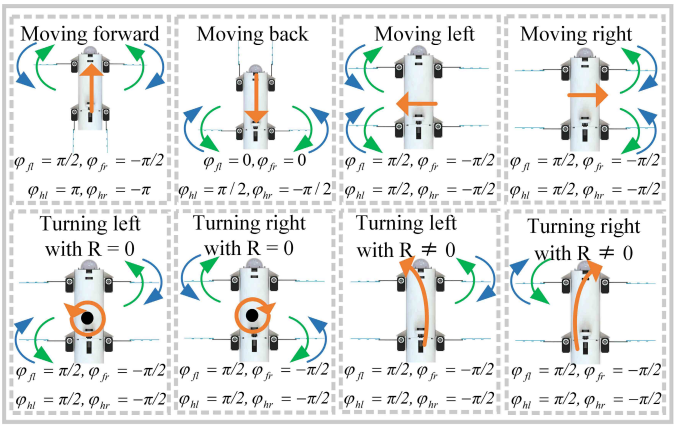

Fig. 8. Multiple swimming gaits. The robot's motion direction is indicated with yellow arrows. The power stroke of the leg is indicated with blue arrows; The recovery stroke of the leg is indicated with green arrows. ϕ is the phase offset. subscript fl means the front left leg, subscript fr means the front right leg, subscript hl means the hind left leg, subscript hr means the hind right leg.

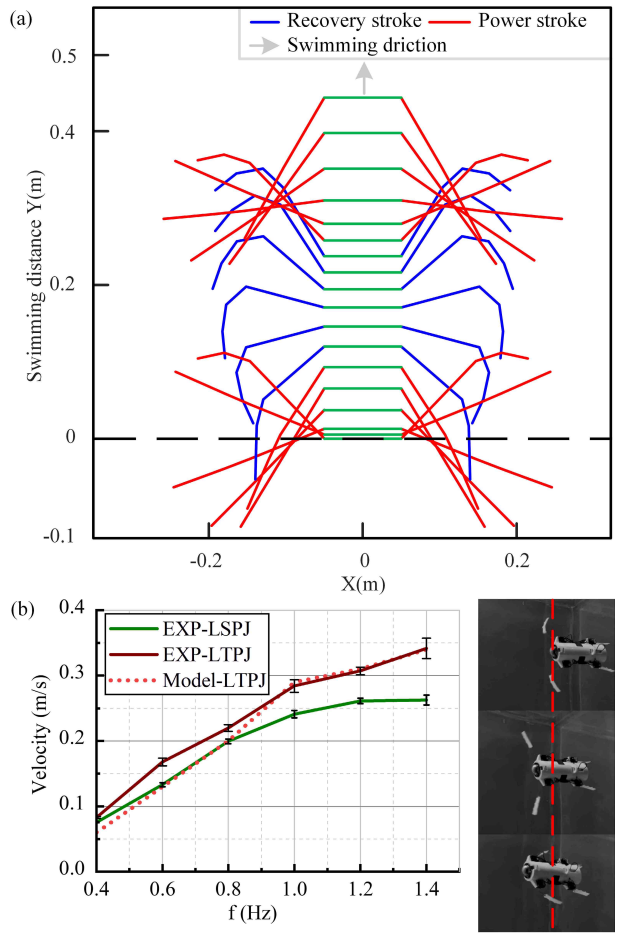

Fig. 9. Simulation and experiment of swimming robot in swimming. (a) simulation of swimming distance (b) comparison of robot with LTPJ and LSPJ. The amplitude is 120°.

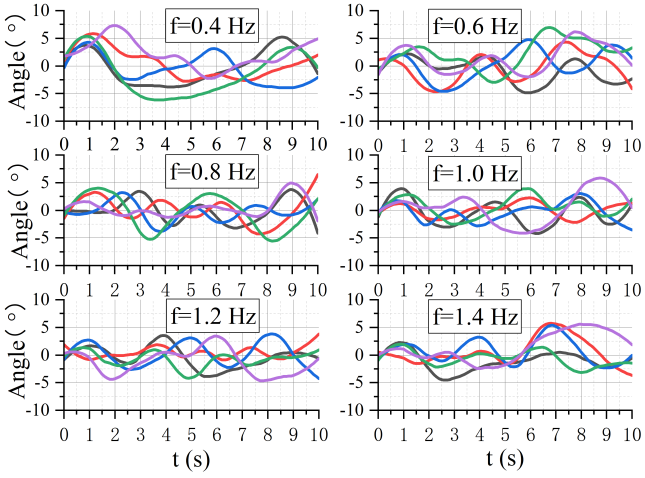

Fig. 10. Yaw stability experiment of the swimming robot.

swimming robot forward, and the symmetric flapping ensures the torque is zero.

Turning left with R = 0: The two legs at the main diagonal are actuated sequentially for smooth turning. The two legs at the secondary diagonal are not driven. Throughout the whole cycle, the net thrust of the two actuated legs is zero, but there is a clockwise torque, allowing the swimming robot to turn left with zero radius.

The remaining gaits are available in the supplemental materials (Movie S1. (1), (2)). The swimming robot moves smoothly in narrow spaces using a variety of gaits, demonstrating excellent stability, adaptability, and maneuverability (Movie S1. (3), (4), (5)). Even if the robot's leg or body collides with an object, it remains undamaged and can still complete its movement (Movie S1. (6), (7)). Overall, the swimming robot presents good performance in narrow spaces.

Fig. 9(a) illustrates the simulated swimming distance of the swimming robot with LTPJ (R-LTPJ). To test the real swimming performance of R-LTPJ and compare it with the robot with LSPJ(R-LSPJ), a water tank experiment was performed, as shown in Fig. 9(b). R-LTPJ's average velocity is higher than that of R-LSPJ, and the gap widens as the frequency increases. Furthermore, the swimming robot can swim faster than many existing swimming robots [38]–[40] in recent research, at a rate of over 0.3 m/s. The high speed and flexibility provide a good foundation for adaptability and maneuverability.

As mentioned in Section II, symmetric lateral force plays a vital role in yaw stability compared to underwater creatures with asymmetric lateral force in forward swimming, such as fish. In this paper, the yaw stability of the swimming robot is tested during forward motion. In this experiment, the actuator has an amplitude of 120°, and the initial phase is shown in Fig. 8. The yaw-angle data are recorded using an IMU. As shown in Fig. 10, the swimming robot's yaw angle is less than half that of a robotic fish with a larger yaw angle in the range of 35° to 180° [41]–[43]. This experiment highlights the superior yaw stability of the swimming robot in forward motion.

VI. Conclusion

This paper explores the potential applications of an omnidirectional swimming robot that achieves excellent stability, adaptability, and maneuverability in narrow areas. The paper describes an articulated and compliant-jointed leg with three passive joints, which provides a larger net thrust and higher propulsion efficiency. The dynamic models of the leg and swimming robot are thoroughly investigated and analyzed, and experiments are performed to validate the dynamic models by measuring deformation, thrust, and efficiency generated by leg flapping in a water tank. Experimental results demonstrate the benefits of the LTPJ compared to LSPJ.

The swimming robot is fabricated and can swim at an average velocity of 0.34 m/s using a pair of front legs with a symmetric flapping approach. The robot is additionally capable of completing multiple gaits, including retreating, lateral, and zero-radius turning motions. Passing and collision experiments also demonstrate that the swimming robot performs exceptionally well in narrow spaces.

There are numerous potential applications for this swimming robot, such as fish farming, underwater ecological exploration, fish school dynamics study, and underwater monitoring. Further research includes studying the control method to improve robotic locomotive accuracy and resistance to turbulence, optimizing the propulsive structure, and refining design parameters.

REFERENCES

[1] Z. Liu and D. Krys, "The use of laser range finder on a robotic platform for pipe inspection," *Mechanical systems and signal processing*, vol. 31, pp. 246–257, 2012.

[2] L. Paull, S. Saeedi, M. Seto, and H. Li, "AUV navigation and localization: A review," *IEEE Journal of Oceanic Engineering*, vol. 39, no. 1, pp. 131–149, 2014.

[3] E. Galceran, R. Campos, N. Palomeras, D. Ribas, M. Carreras, and P. Ridao, "Coverage Path Planning with Real-time Replanning and Surface Reconstruction for Inspection of Three-dimensional Underwater Structures using Autonomous Underwater Vehicles," *Journal of Field Robotics*, vol. 32, no. 7, pp. 952–983, 2015.

[4] J. D. Hernández, E. Vidal, M. Moll, N. Palomeras, M. Carreras, and L. E. Kavraki, "Online motion planning for unexplored underwater environments using autonomous underwater vehicles," *Journal of Field Robotics*, vol. 36, no. 2, pp. 370–396, 2019.

[5] J. Li, "Position control based on the estimated bending force in a soft robot with tunable stiffness," *Mechanical Systems and Signal Processing*, vol. 134, p. 106335, 2019.

[6] A. D. Marchese and D. Rus, "Design, kinematics, and control of a soft spatial fluidic elastomer manipulator," *The International Journal of Robotics Research*, vol. 35, no. 7, pp. 840–869, 2016.

[7] M. Christie, S. Sun, D. Ning, H. Du, S. Zhang, and W. Li, "A highly stiffness-adjustable robot leg for enhancing locomotive performance," *Mechanical Systems and Signal Processing*, vol. 126, pp. 458–468, 2019.

[8] F. Berlinger, M. Duduta, H. Gloria, D. Clarke, R. Nagpal, and R. Wood, "A Modular Dielectric Elastomer Actuator to Drive Miniature Autonomous Underwater Vehicles," in *2018 IEEE International Conference on Robotics and Automation (ICRA)*, 2018.

[9] Y. Wang, X. Yang, Y. Chen, D. K. Wainwright, C. P. Kenaley, Z. Gong, Z. Liu, H. Liu, J. Guan, T. Wang *et al.*, "A biorobotic adhesive disc for underwater hitchhiking inspired by the remora suckerfish," *Science Robotics*, vol. 2, no. 10, p. eaan8072, 2017.

[10] Y. Chen, N. Sun, D. Liang, Y. Qin, and Y. Fang, "A neuroadaptive control method for pneumatic artificial muscle systems with hardware experiments," *Mechanical Systems and Signal Processing*, vol. 146, p. 106976, 2021.

[11] C. A. Aubin, S. Choudhury, R. Jerch, L. A. Archer, J. H. Pikul, and R. F. Shepherd, "Electrolytic vascular systems for energy-dense robots," *Nature*, vol. 571, no. 7763, pp. 51–57, Jul 2019.

[12] R. Wang, S. Wang, Y. Wang, L. Cheng, and M. Tan, "Development and motion control of biomimetic underwater robots: A survey," *IEEE Transactions on Systems, Man, and Cybernetics: Systems*, vol. 52, no. 2, pp. 833–844, 2022.

[13] F. Berlinger, M. Gauci, and R. Nagpal, "Implicit coordination for 3d underwater collective behaviors in a fish-inspired robot swarm," *Science Robotics*, vol. 6, no. 50, p. eabd8668, 2021.

[14] C. Huang, Z. Lai, X. Wu, and T. Xu, "Multimodal locomotion and cargo transportation of magnetically actuated quadruped soft microrobots," *Cyborg and Bionic Systems*, vol. 2022, p. 0004, 2023.

[15] Q. Zhong, J. Zhu, F. E. Fish, S. J. Kerr, A. Downs, H. Bart-Smith, and D. Quinn, "Tunable stiffness enables fast and efficient swimming in fish-like robots," *Science Robotics*, vol. 6, no. 57, p. eabe4088, 2021.

[16] K. A. Morgansen, B. I. Triplett, and D. J. Klein, "Geometric methods for modeling and control of free-swimming fin-actuated underwater vehicles," *IEEE Transactions on Robotics*, vol. 23, no. 6, pp. 1184–1199, 2007.

[17] A. Simha, R. Gkliva, . Kotta, and M. Kruusmaa, "A flapped paddle-fin for improving underwater propulsive efficiency of oscillatory actuation," *IEEE Robotics and Automation Letters*, vol. 5, no. 2, pp. 3176–3181, 2020.

[18] J. Fan, S. Wang, Q. Yu, and Y. Zhu, "Swimming performance of the frog-inspired soft robot," *Soft Robotics*, vol. 7, no. 5, pp. 615–626, 2020.

[19] H.-J. Kim, S.-H. Song, and S.-H. Ahn, "A turtle-like swimming robot using a smart soft composite (SSC) structure," *Smart Materials and Structures*, vol. 22, no. 1, p. 014007, 2013.

[20] M. Sfakiotakis, A. Kazakidi, and D. P. Tsakiris, "Octopus-inspired multiarm robotic swimming," *Bioinspiration & Biomimetics*, vol. 10, no. 3, p. 035005, 2015.

[21] S. Wang, B. Huang, D. McCoul, M. Li, L. Mu, and J. Zhao, "A soft breaststroke-inspired swimming robot actuated by dielectric elastomers," *Smart Materials and Structures*, vol. 28, no. 4, p. 045006, 2019.

[22] J. L. Tangorra, A. P. Mignano, G. N. Carryon, and J. C. Kahn, "Biologically derived models of the sunfish for experimental investigations of multi-fin swimming," in *2011 IEEE/RSJ International Conference on Intelligent Robots and Systems*, 2011, pp. 580–587.

[23] N. Palomeras, N. Hurtos, E. Vidal, and M. Carreras, "Autonomous Exploration of Complex Underwater Environments Using a Probabilistic Next-Best-View Planner," *IEEE Robotics and Automation Letters*, vol. 4, no. 2, pp. 1619–1625, 2019.

[24] S. Behbahani and X. Tan, "Design and Modeling of Flexible Passive Rowing Joint for Robotic Fish Pectoral Fins," *IEEE Transactions on Robotics*, vol. 32, no. 5, pp. 1119–1132, 2016.

[25] M. Sharifzadeh and D. M. Aukes, "Curvature-induced buckling for flapping-wing vehicles," *IEEE/ASME Transactions on Mechatronics*, vol. 26, no. 1, pp. 503–514, 2021.

[26] M. Jiang, Q. Yu, and N. Gravish, "Vacuum induced tube pinching enables reconfigurable flexure joints with controllable bend axis and stiffness," *2021 IEEE 4th International Conference on Soft Robotics, RoboSoft 2021*, pp. 315–320, 2021.

[27] D. Krishnamurthy, G. Katsikis, A. Bhargava, and M. Prakash, "Schistosoma mansoni cercariae swim efficiently by exploiting an elastohydrodynamic coupling," *Nature Physics*, vol. 13, no. 3, pp. 266–271, 2017.

[28] K. Diaz, T. L. Robinson, Y. O. Aydin, E. Aydin, D. I. Goldman, and K. Y. Wan, "A minimal robophysical model of quadriflagellate self-propulsion," *Bioinspiration and Biomimetics*, vol. 16, no. 6, 2021.

[29] S. P. Liu, B. Wipfler, and R. G. Beutel, "The unique locomotor apparatus of whirligig beetles of the tribe Orectochilini (Gyrinidae, Coleoptera)," *Journal of Zoological Systematics and Evolutionary Research*, vol. 56, no. 2, pp. 196–208, 2018.

[30] Z. Xu, S. C. Lenaghan, B. E. Reese, X. Jia, and M. Zhang, "Experimental Studies and Dynamics Modeling Analysis of the Swimming and Diving of Whirligig Beetles (Coleoptera: Gyrinidae)," *PLoS Computational Biology*, vol. 8, no. 11, 2012.

[31] W. Nachtigall, "Chapter 6 - locomotion: Mechanics and hydrodynamics of swimming in aquatic insects," in *The Physiology of Insecta (Second Edition)*, second edition ed., M. ROCKSTEIN, Ed. Academic Press, 1974, pp. 381–432.

[32] M. H. Dickinson, C. T. Farley, R. J. Full, M. A. R. Koehl, R. Kram, and S. Lehman, "How animals move: An integrative view," *Science*, vol. 288, no. 5463, pp. 100–106, 2000.

[33] J. Wang, P. K. McKinley, and X. Tan, "Dynamic modeling of robotic fish with a base-actuated flexible tail," *Journal of dynamic systems, measurement, and control*, vol. 137, no. 1, 2015.

[34] Q. Zuo, Y. Xu, F. Xie, H. Fang, K. He, Y. Zhong, and Z. Li, "Dynamic Modeling of a Novel Kind of Rigid-Soft Coupling Biomimetic Robotic Fish," *Journal of Intelligent and Robotic Systems: Theory and Applications*, vol. 105, no. 2, 2022.

[35] M. Zefran and F. Bullo, "Lagrangian dynamics," *Robotics and Automation Handbook*, 2005:5–1.

[36] J. S. Palmisano, R. Ramamurti, J. D. Geder, M. Pruessner, W. C. Sandberg, and B. Ratna, "How to maximize pectoral fin efficiency by control of flapping frequency and amplitude," in *18th International Symposium on Unmanned Untethered Submersible Technology*, 2013.

[37] A. Banerjee and S. Nagarajan, "Efficient simulation of large overall motion of beams undergoing large deflection," *Multibody System Dynamics*, vol. 1, no. 1, pp. 113–126, 1997.

[38] B. Kwak, S. Choi, and J. Bae, "Development of a stiffness-adjustable articulated paddle and its application to a swimming robot," *Advanced Intelligent Systems*, p. 2200348, 2023.

[39] M. Sharifzadeh, Y. Jiang, and D. M. Aukes, "Reconfigurable curved beams for selectable swimming gaits in an underwater robot," *IEEE Robotics and Automation Letters*, vol. 6, no. 2, pp. 3437–3444, 2021.

[40] V. A. Pham, T. T. Nguyen, B. R. Lee, and T. Q. Vo, "Dynamic Analysis of a Robotic Fish Propelled by Flexible Folding Pectoral Fins," *Robotica*, vol. 38, no. 2020, pp. 699–718, 2019.

[41] M. Ye, H. Wang, A. Yazdani, S. He, Z. Ping, and W. Xu, "Discrete-time integral terminal sliding mode-based speed tracking control for a robotic fish," *Nonlinear Dynamics*, vol. 105, no. 1, pp. 359–370, Jul 2021.

[42] C. Zhou, Z.-G. Hou, Z. Cao, S. Wang, and M. Tan, "Motion modeling and neural networks based yaw control of a biomimetic robotic fish," *Information Sciences*, vol. 237, pp. 39–48, 2013.

[43] X. Zheng, W. Wang, L. Li, and G. Xie, "Artificial lateral line based relative state estimation between an upstream oscillating fin and a downstream robotic fish," *Bioinspiration & Biomimetics*, vol. 16, no. 1, p. 016012, Nov 2020.